Electrochemistry
The Electrochemical Society of Japan
Received: January 21, 2025
Accepted: February 24, 2025
Published online: February 27, 2025
Issued: March 29, 2025
https://doi.org/10.5796/electrochemistry.25-00015
https://doi.org/10.50892/data.electrochemistry.28490150
Article
Electrochemistry, 93(3), 037009 (2025)

Electrochemical Lithiation Mechanism of Nickel Silicide Electrode

OPEN ACCESS

Yasuhiro DOMI,[a,c,*,§] Hiroyuki USUI,[a,c,§] Takumi ANDO,[b,c] Ryuto TANAKA,[b,c,§§] Kazuma GOTOH,[d,§] Takeo HOSHI,[e] Kei NISHIKAWA,[f,§] and Hiroki SAKAGUCHI[a,c,*,§§§]

[a] Department of Chemistry and Biotechnology, Graduate School of Engineering, Tottori University, 4-101 Minami, Koyama-cho, Tottori 680-8552, Japan
[b] Course of Chemistry and Biotechnology, Department of Engineering, Graduate School of Sustainability Science, Tottori University, 4-101 Minami, Koyama-cho, Tottori 680-8552, Japan
[c] Center for Research on Green Sustainable Chemistry, Tottori University, 4-101 Minami, Koyama-cho, Tottori 680-8552, Japan
[d] Center for Nano Materials and Technology, Japan Advance Institute of Science and Technology, 1-1 Asahidai, Nomi, Ishikawa 923-1292, Japan
[e] Plasma Quantum Process Unit, National Institute for Fusion Science, 322-6 Oroshi, Toki-shi, Gifu 509-5292, Japan
[f] Center for Green Research on Energy and Environmental Materials, National Institute for Materials Science (NIMS), 1-1 Namiki, Tsukuba 305-0044, Japan

*Corresponding authors: domi@tottori-u.ac.jp (Y. D.), Tel/Fax: +81-857-31-5249, sakaguch@tottori-u.ac.jp (H. S.), Tel/Fax: +81-857-31-5265

ABSTRACT

Pure silicide electrodes have attracted attention as a promising anode material in lithium-ion batteries using certain ionic liquid electrolytes. However, the reaction mechanisms of silicide electrodes, particularly the lithiation sites in the crystal lattice and the reaction sites (bulk versus surface), remain unclear. Here, we investigated the electrochemical lithiation mechanism of a nickel silicide ($NiSi_2$) electrode. X-ray diffraction, transmission electron microscopy, and other techniques revealed that $NiSi_2$ phase did not separate and no lithiation of Si generated from $NiSi_2$ occurred. In contrast, ^{7}Li magic angle spinning nuclear magnetic resonance demonstrated that stable deposition–dissolution of Li metal did not occur on the $NiSi_2$ electrode, and electrochemical lithiation of $NiSi_2$ proceeded. Additionally, we investigated the lithiation sites using computational chemistry. The peak positions in the nuclear magnetic resonance spectra differed from those predicted using the calculated valence electron numbers. This resulted from an increase in conduction electrons near the Fermi energy associated with the amount of Li stored in the $NiSi_2$ crystal lattice, followed by a Knight shift.

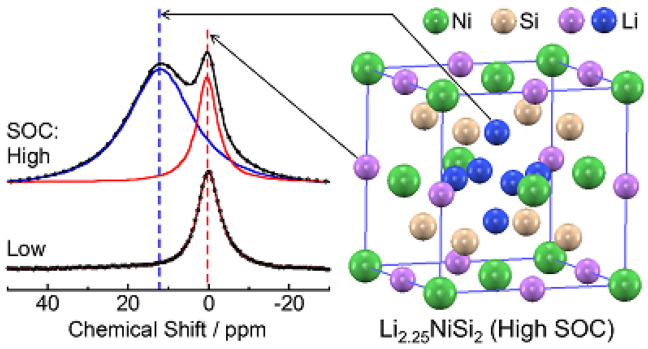

Keywords : Reaction Mechanism, Lithiation Site, Ionic-liquid Electrolyte, Knight Shift

1. Introduction

Silicon (Si) has attracted attention as a promising anode material in lithium-ion batteries (LIBs) with gravimetric high-energy density because of its high theoretical capacity of 3600 mA h g^{-1} in the crystalline $Li_{3.75}Si$ phase at room temperature.[1–4] The development of high-performance LIBs is essential to realize a decarbonized society, and the practical application of Si anodes is gaining momentum.[5–8] However, the poor cycling stability caused by large volume changes in Si during alloying (charge) and dealloying (discharge) with lithium (Li) prevents its practical application. We previously investigated how to improve the anode properties of pure Si electrodes by doping impurities into Si,[9,10] fabricating composites with materials that compensate for the Si defects,[11–16] and prelithiation.[17,18] Additionally, we have developed Si-specific interface observation methods.[19–21]

In contrast, we investigated the feasibility of pure silicide (MSi_x, M: transition metal) electrodes, which are Si compounds with metals. MSi_x electrodes have not received much attention because they have not shown good cycling performance in conventional organic liquid electrolytes.[11] We also discovered that the MSi_x electrodes achieved very high capacity and excellent cycling stability in a particular ionic liquid electrolyte of 1 mol dm^{-3} (M) Li bis(fluorosulfonyl)amide (LiFSA) in *N*-methyl-*N*-propylpyrrolidinium bis(fluorosulfonyl)amide (Py13-FSA).[22] Furthermore, most MSi_x have high density, therefore, high volumetric reversible capacity can be expected.[23]

The electrochemical lithiation mechanism of some MSi_x electrodes has been reported; lithiation of Si resulting from the phase separation of MSi_x occurred.[24–26] However, the lithiation-

§ECSJ Active Member
§§ECSJ Student Member
§§§ECSJ Fellow
Y. Domi orcid.org/0000-0003-3983-2202
H. Usui orcid.org/0000-0002-1156-0340
K. Gotoh orcid.org/0000-0002-8197-5701
T. Hoshi orcid.org/0000-0002-2487-5245
K. Nishikawa orcid.org/0000-0002-7718-7606
H. Sakaguchi orcid.org/0000-0002-4125-7182

delithiation of MSi_x itself is expected to occur based on the dissolution enthalpy, rather than the phase separation of MSi_x. For example, the dissolution enthalpy of Fe-Si, Ni-Si, and La-Si is −67, −86, and −285 kJ mol^{-1}, respectively.[27] Larger negative value of the enthalpy indicates that these silicides are thermodynamically stable. In contrast, the dissolution enthalpy of Si-Li has been reported to be −51 kJ mol^{-1}.[27] Because Si has a higher affinity for transition metals than for Li, it is inferred that MSi_x is less likely to be decomposed during charge-discharge cycling.

We previously investigated the reaction behavior of an iron silicide ($FeSi_2$) electrode using X-ray diffraction (XRD), Raman spectroscopy, transmission electron microscopy (TEM), energy-dispersive X-ray spectroscopy (EDS), and solid-state ^{7}Li magic angle spinning (MAS) nuclear magnetic resonance (NMR).[28] We concluded that the $FeSi_2$ electrode alloyed with Li; nevertheless, lithiation sites in the $FeSi_2$ crystal lattice and reaction locations (bulk or surface) remained unclear. It is also unclear whether the reaction behavior is identical when different *M* is used. In the present study, the electrochemical lithiation mechanism of a nickel silicide ($NiSi_2$) electrode in 1 M LiFSA/Py13-FSA was investigated using the above analytical methods. Additionally, we attempted to identify the lithiation sites using density functional theory for first-principles calculations. We predicted the NMR peak positions based on the calculated valence electron numbers and discussed the Knight shift, which occurs when conduction electrons near the Fermi energy increase according to the quantity of Li stored in the $NiSi_2$ crystal lattice.

2. Experimental

2.1 Sample preparation and electrode fabrication

$NiSi_2$ was prepared by a mechanical alloying (MA) method. A mixture of silicon (99.9 %, FUJIFILM Wako Pure Chemical Corp., Ltd.) and nickel (99.9 %, Nilaco Corp.) powders was put in a ZrO_2 container together with ZrO_2 balls. Dry Ar gas was filled the container. The Si/Ni molar ratio was 2.0 and the weight ratio of the mixture to the balls was approximately 1 : 15. High-energy planetary ball mill apparatus (P-6, Fritch) was used for the MA process performing with a rotary speed of 380 rpm at room temperature for 20 h. The crystal structure of prepared powder was verified by XRD (Ultima IV, Rigaku) with Cu-Kα radiation and obtained XRD pattern was identified using the Inorganic Crystal Structure Database (ICSD).

An $NiSi_2$ electrode was fabricated by slurry coating method for ^{7}Li MAS NMR and XRD measurements. Acetylene black (AB), styrene-butadiene rubber (SBR), and carboxymethyl cellulose (CMC) were used as the conductive agent, binder, and thickener, respectively. The ratio of $NiSi_2$/AB/SBR/CMC was 70/15/5/10 wt%. 4 g of deionized water was used as a dispersing agent for 1 g of the mixture. The prepared slurry was coated on a copper current collector and was dried at 120 °C. In contrast, an $NiSi_2$ gas-deposition (GD) electrode was prepared for TEM and Raman microscopy measurements. The GD electrode was used instead of the slurry electrode to investigate changes in the active material itself in TEM observation, and because of the possibility that CMC-derived peaks might appear at 500 cm^{-1}, where Si-derived peaks appear in the Raman spectra.[29] The GD method requires no conductive agent or binder. He gas (99.9999 %) was used as a carrier gas and the deposited amount of $NiSi_2$ on the current collector was approximately 30 µg. Other detail conditions of GD method were described in our previous paper.[19]

2.2 Cell assembly and charge–discharge testing

A 2032-type coin cell was assembled using the $NiSi_2$ electrode, a glass fiber filter (Whatman GF/A), and a Li metal sheet (99.90 %, thickness: 1 mm, Rare Metallic Co., Ltd.) as the working electrode, the separator, and the counter electrode, respectively. We used 1 M LiFSA/Py13-FSA as an ionic-liquid electrolyte. Cell assembly and electrolyte preparation were conducted in an Ar-filled glovebox (Miwa MFG, DBO-2.5LNKP-TS) with an oxygen content less than 1 ppm and a dew point below −90 °C.

Galvanostatic charge–discharge testing was performed using an electrochemical measurement system (HJ-1001SM8A or HJ-1001SD8, MEIDEN HOKUTO, Co., Ltd.) in the potential range between 0.005 and 2.000 V vs. Li^+/Li at 30 °C. The current density was set at 50 mA g^{-1}. After the testing of the cell using slurry electrode for 4 cycles, the cell was charged to adjust the state of charge (SOC) at the fifth cycle for each point of the ^{7}Li MAS NMR measurement. The potential was maintained at each point in Fig. S1a for 12 h. The charge capacity at the first cycle was higher than that after the second cycle due to the formation of a surface film, whereas the charge–discharge capacity and the corresponding curve were almost the same after the second cycle (Fig. S1b). The testing of the cell using GD electrode was carried out for 5 cycles. The Coulombic efficiency of the slurry electrode was higher than that of the GD electrode, and hence, a side reaction of AB with Li^+ should not occur.

2.3 ^{7}Li MAS NMR measurement and TEM observation

The coin cell was disassembled in the Ar-filled glovebox after the above–mentioned charge–discharge testing. The slurry electrode was washed thoroughly with diethyl carbonate (DEC, Kishida Chemical Co., Ltd.) and was dried. The active material layer including $NiSi_2$, AB, SBR, and CMC was exfoliated from Cu substrate using a spatula. The resulting powder was packed in a 3.2 mmϕ sample tube for the NMR measurement. ^{7}Li MAS NMR spectra of $NiSi_2$ at each SOC were obtained using an NMR system (11.7 T magnet, DD2 Agilent Technologies Inc.) at a MAS frequency of 14 kHz. The chemical shifts were referenced to a 1 M aqueous LiCl solution. The peak fitting of NMR spectra was performed by Origin Pro 8.5.0J (LightStone) software.

Removed $NiSi_2$ GD electrode from the coin cell was washed with propylene carbonate and DEC before drying. The electrode was sliced into thin sections using focused ion beam scanning electron microscopy (FIB-SEM, SMF2000, Hitach High-Tech Science Corp.). The electrode surface was coated with carbon to protect it from damage by the Ga ion beam. The sliced electrode was not exposed to the atmosphere until it was introduced into the chamber of the TEM instrument (JEM-ARM200F, JEOL, Co., Ltd.) using a transfer vessel. TEM observation was performed with acceleration voltage of 200 KV and energy-dispersive X-ray spectroscopy (EDS) was carried out with 10 scans.

2.4 First-principles calculation

We used a commercially available Advance/PHASE software package (Advance Soft Corp.) using plane wave expansion and pseudopotentials based on density functional theory for first-principles calculation. Projector augmented wave (PAW) and generalized gradient approximation (GGA) were utilized as calculation method and exchange–correlation energy function. We used the *k*-space integrations of 5 × 5 × 5 *k*-point mesh. We also used a cut-off energy of 340 eV for wave function (total density of state: total DOS) and 3060 eV for charge density (Bader analysis), which corresponds to 12.5 and 112.5 Hartree, respectively (1 Hartree equals to 27.2114 eV). The valence electron number of Li was estimated by the Bader analysis.

3. Results and Discussion

3.1 Possible electrochemical lithiation mechanisms of the $NiSi_2$ electrode

Figure 1 shows a schematic diagram of the possible electrochemical lithiation mechanisms for $NiSi_2$ electrodes. In the first mechan-

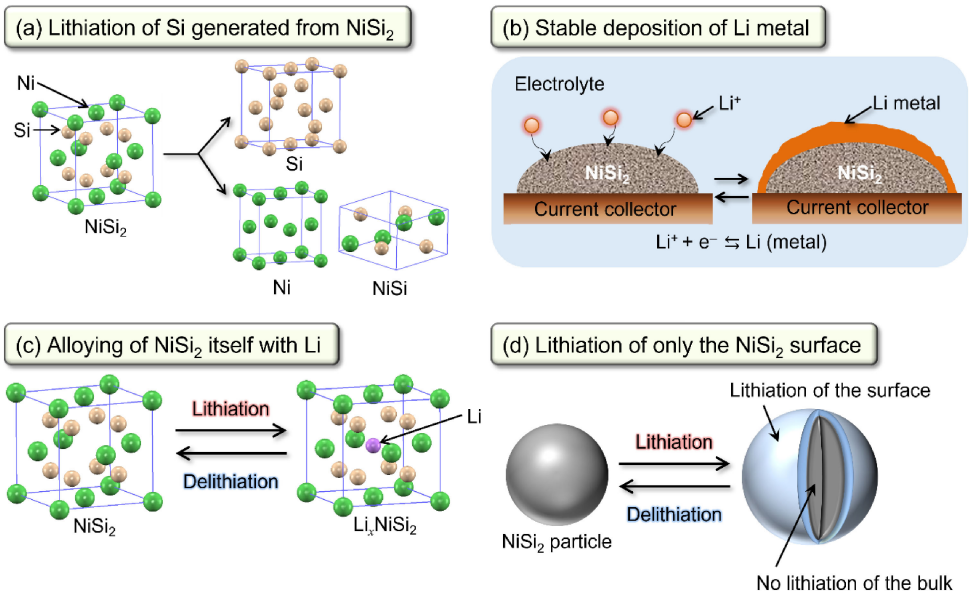

Figure 1. Schematic diagram of possible electrochemical lithiation mechanisms for $NiSi_2$ electrodes: (a) lithiation of Si generated from $NiSi_2$, (b) stable deposition of Li metal on the $NiSi_2$, (c) alloying of $NiSi_2$ with Li, and (d) lithiation of only the $NiSi_2$ surface.

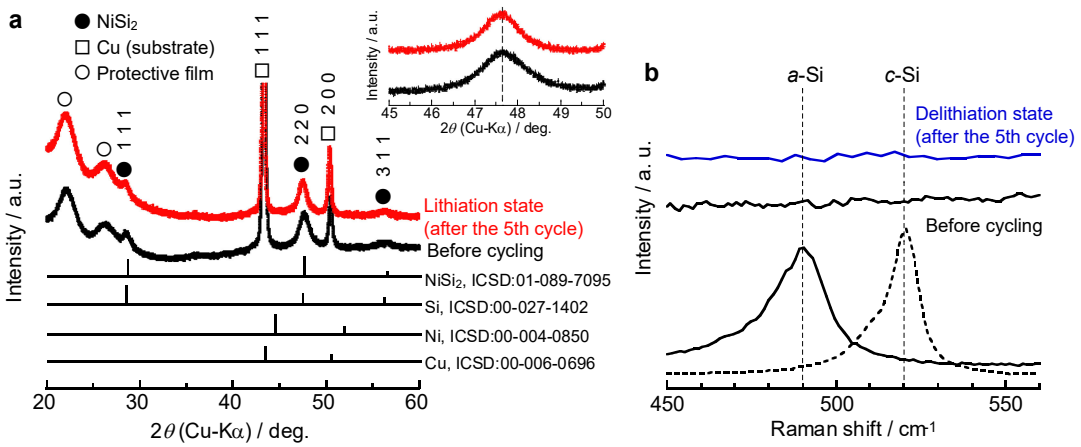

Figure 2. (a) XRD patterns of the pristine $NiSi_2$ and lithiated $NiSi_2$ electrode after the fifth charge–discharge cycle and (b) Raman spectra of the $NiSi_2$ electrode before and after the fifth cycle with those of *a*-Si and *c*-Si.

ism, the $NiSi_2$ phase separates into Si and Ni and/or Si-poor nickel silicides (NiSi, Ni_2Si, and Ni_3Si) phases, generating Si alloys with Li (Fig. 1a). The following reactions are expected to occur:

$$NiSi_2 + xLi^+ + xe^- \rightarrow Ni + 2Li_xSi \quad (1)$$

$$NiSi_2 + xLi^+ + xe^- \rightarrow NiSi + Li_xSi \quad (2)$$

$$2NiSi_2 + xLi^+ + xe^- \rightarrow Ni_2Si + 3Li_xSi \quad (3)$$

$$3NiSi_2 + xLi^+ + xe^- \rightarrow Ni_3Si + 5Li_xSi \quad (4)$$

In the second possible mechanism, deposition and dissolution of Li metal occur on the $NiSi_2$ electrode (Fig. 1b). Because the charge–discharge cycle stability of the electrode in 1 M Py13-FSA is good, Li dendrites should not be produced. The $NiSi_2$ electrode may act as a foothold for stable Li deposition–dissolution. In the third possible mechanism, the $NiSi_2$ itself alloys and dealloys with Li as follows (Fig. 1c):

$$NiSi_2 + xLi^+ + xe^- \rightarrow Li_xNiSi_2 \quad (5)$$

In the fourth possible mechanism, the bulk of the $NiSi_2$ particle is not lithiated and only the surface alloys with Li (Fig. 1d). This is a new hypothesis that arose while investigating the above three possibilities. Herein, each of these four mechanisms was examined.

3.2 Lithiation of Si generated from $NiSi_2$ phase separation

The active material of $NiSi_2$ was successfully synthesized using a mechanical alloying method and characterized using XRD, Raman spectroscopy, field-emission scanning electron microscopy (FE–SEM), and a particle size distribution analyzer (Figs. S2 and S3). To verify whether the $NiSi_2$ phase separates into Si and Ni and/or Si-poor nickel silicides (Fig. 1a), we investigated the change in the $NiSi_2$ crystal structure during charge–discharge cycling. Figure 2a displays the XRD pattern of the fully lithiated $NiSi_2$ electrode during the fifth cycle. For comparison, the result of the pristine $NiSi_2$ electrode is also shown. All peaks except those derived from the copper substrate and the protective film were attributed to $NiSi_2$. No new peaks derived from Si, Ni, Si-poor nickel silicides (NiSi, Ni_2Si, and Ni_3Si), or lithium silicides (Li_xSi) appeared. The crystallinity of Si decreases after charge–discharge cycling, i.e., crystalline Si (*c*-Si) changes to amorphous Si (*a*-Si).[19,30] Because XRD can not detect *a*-Si, Raman spectroscopy, which can detect Si of any crystallinity,

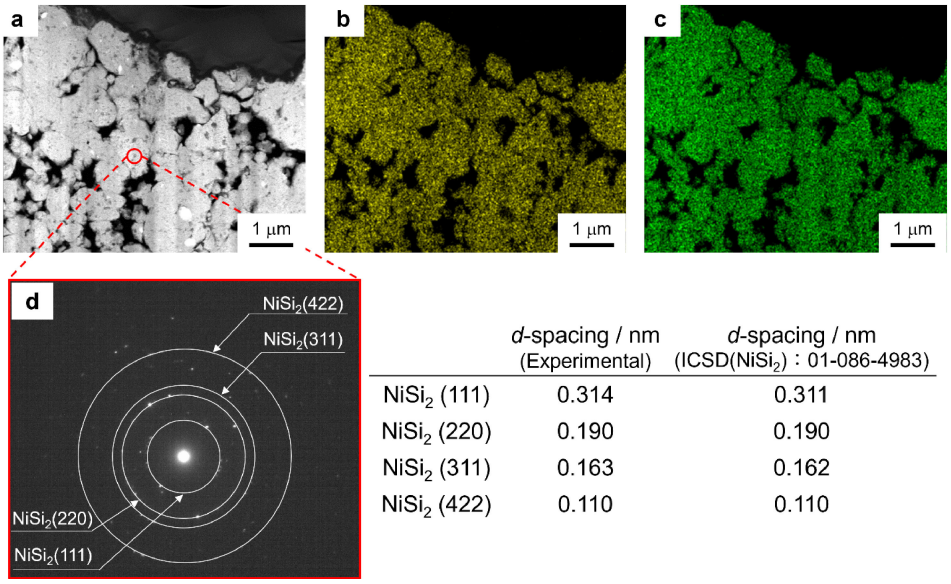

	d-spacing / nm (Experimental)	*d*-spacing / nm (ICSD($NiSi_2$) : 01-086-4983)
$NiSi_2$ (111)	0.314	0.311
$NiSi_2$ (220)	0.190	0.190
$NiSi_2$ (311)	0.163	0.162
$NiSi_2$ (422)	0.110	0.110

Figure 3. (a) TEM image of delithiated $NiSi_2$ after the fifth cycle and the corresponding EDS maps of (b) Ni and (c) Si. (d) SAED pattern with the corresponding *d*-spacings are also shown.

was used to investigate whether elemental Si was generated from $NiSi_2$ (Fig. 2b). No Si of any crystallinity was detected, indicating that phase separation of $NiSi_2$ did not occur during charge–discharge cycling. However, if the $NiSi_2$ phase separates into Si and Ni and/or Si-poor $NiSi_x$ ($x = 1$, $1/2$, and $1/3$) phases at the extreme surface and ultrafine Si particles (diameter ≤ 100 nm) are formed, Raman spectroscopy cannot detect the particles because of the definite resolution. Hence, we used TEM to observe a cross-section of the $NiSi_2$ electrode after the charge–discharge cycling.

Figure 3a shows a TEM image of the delithiated $NiSi_2$ electrode after the fifth charge–discharge cycle. The corresponding EDS maps of Ni and Si, the selective area electron diffraction (SAED) pattern, and the obtained *d*-spacing values are also shown (Figs. 3b–3d, respectively). Ni and Si elements were uniformly distributed, and no ultrafine Si particles appeared. The SAED and *d*-spacing results showed that a Si phase was not formed, and the active material layer remained $NiSi_2$ after cycling. Figures 2 and 3 show that no phase separation of $NiSi_2$ occurred and a pure Si phase was not generated; thus, the electrochemical lithiation mechanism of the $NiSi_2$ electrode could not be explained by the first hypothesis (Fig. 1a).

3.3 Li Deposition on $NiSi_2$

Figure 4 provides the ^{7}Li MAS NMR spectrum of the fully lithiated $NiSi_2$ electrode during the fifth cycle. Peaks with asterisks were assigned to spinning sidebands, which is outside the scope of this discussion. Li metal peak, including Li dendrites, appeared at approximately 260 ppm,[31,32] such peak was not detected. The same phenomenon was previously confirmed on a $FeSi_2$ electrode.[28] In contrast, main peaks at approximately 0 ppm were confirmed, as discussed below. Therefore, the $NiSi_2$ electrode did not serve as a foundation for stable Li deposition–dissolution; thus, the electrochemical lithiation mechanism of the $NiSi_2$ electrode could not be explained by the second hypothesis (Fig. 1b).

3.4 Lithiation and delithiation of $NiSi_2$ itself

Figure 5a provides the ^{7}Li MAS NMR spectra of the $NiSi_2$ electrodes at each state of charge (SOC) during the fifth cycle. At an SOC of 0 %, a peak defined as Peak A appeared at approximately 0 ppm. Peak A at 0 % SOC could not be attributed to Li stored in the $NiSi_2$ because the electrode potential was too high (Fig. S1). Therefore, Peak A was attributed to either Li salt (LiFSA)

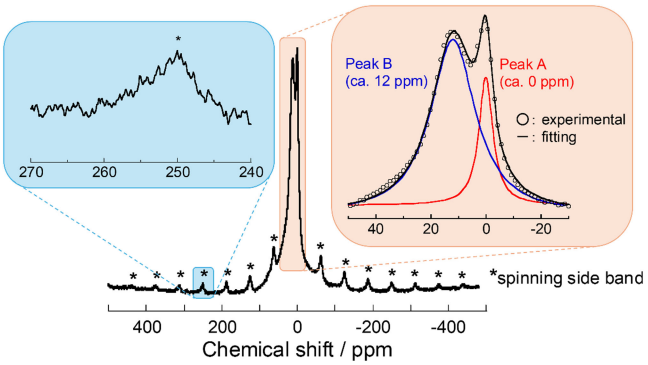

Figure 4. ^{7}Li MAS NMR spectrum of $NiSi_2$ at an SOC of 100 % during the fifth cycle. Magnified views at approximately 0 ppm and approximately 260 ppm are also shown.

in the electrolyte (LiFSA shows extremely clear NMR peak at approximately −1 ppm) or Li contained in the surface film formed on the $NiSi_2$ electrode by reductive decomposition of the electrolyte. Because the $NiSi_2$ electrode had been carefully cleaned with DEC, no LiFSA was expected to remain on the surface. Additionally, Li-containing compounds (i.e., lithium hydroxide and lithium fluoride), which were components of the surface film, show NMR peaks at approximately 0 ppm.[33–35] Hence, Peak A at 0 % SOC was assigned to Li in the surface film.

At SOCs from 20 % to 40 %, the intensity of Peak A increased (Figs. 5a and 5b), although the peak position did not change (Fig. 5c). The Coulombic efficiency was as high as 97.7 % during the fifth cycle (Fig. S4); thus the increase in Peak A at SOCs between 20 % and 40 % was not attributed to the growth of the surface film. Grey et al. reported that various Li–Si alloy phases (Li_xSi, $x = 1.71$, 2.33, 3.25, and 3.75) generate ^{7}Li NMR peaks between 18.0 ppm and 6.0 ppm, which were assigned to Li near small Si clusters and isolated Si.[36,37] The peak centered at 18.0 ppm shifted toward a lower chemical shift (higher magnetic field) as *x* increased. The peak position of Peak A did not correspond to the above Li–Si alloys; hence, Peak A between 20 % and 40 % SOC was assigned to Li stored in $NiSi_2$.

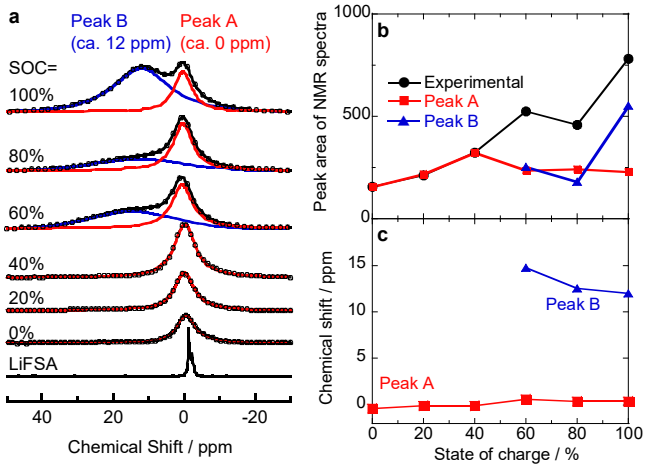

Figure 5. (a) ^{7}Li MAS NMR spectra of $NiSi_2$ at various SOCs during the fifth cycle in 1 M LiFSA/Py13-FSA at 50 mA g^{-1} after pre-cycling. Correlation between the SOC and the (b) peak area and (c) chemical shift. Peak fitting data are shown as red and blue lines in part (a).

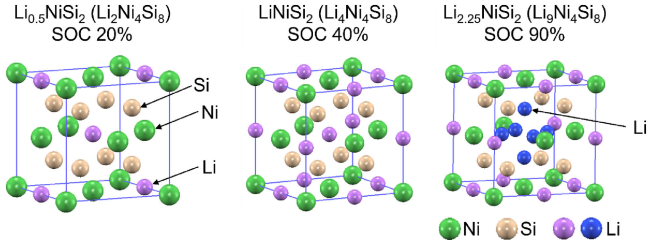

Figure 6. Crystal structure of Li_yNiSi_2 ($y = 0.5$, 1.0, and 2.25).

Table 1. Number of valence electrons and Li atoms in Li_yNiSi_2 ($y = 0.5$, 1.0, and 2.25).

y in Li_yNiSi_2	SOC	Valence electron numbers of Li	Number of Li atoms	Ball color in Fig. 6
0.5	20	0.20	2	Purple
1.0	40	0.20	4	Purple
2.25	90	0.16	3	Purple
		0.28	6	Blue

At a high SOC of 60 %, a shoulder appeared at approximately 15 ppm, which was defined as Peak B. Peak B increased with the increase in SOC and shifted toward a lower chemical shift. The appearance of both peaks denoted two possibilities: (i) Li was stored in two different forms (i.e., Si and NiSi), or (ii) Li existed in two different chemical environments within the same material ($NiSi_2$). Because the $Li_{2.33}Si$ phase produces an NMR peak at approximately 16.5 ppm,[36] Peak B could arise from this phase. However, Figs. 2 and 3 revealed the absence of Si before and after charge–discharge cycling. Thus, the occurrence of Peaks A and B indicated that Li existed in two different chemical environments within $NiSi_2$. Consequently, the increase in the peak area between SOCs of 20 % and 100 % can be attributed to the lithiation of the $NiSi_2$ electrode according to Eq. 5; thus, the electrochemical lithiation mechanism of the $NiSi_2$ electrode can be explained by the third hypothesis (Fig. 1c). The details of the lithiation sites are described in the next section.

When Li_yNiSi_2 forms after cycling, the XRD peaks of $NiSi_2$ shift toward a lower angle because of $NiSi_2$ lattice expansion caused by Li storage. It was also confirmed that the $NiSi_2$ lattice volume expanded with an increase in the amount of Li stored in the $NiSi_2$ crystal lattice by first-principles calculations (Table S1, the crystal structure was optimized); however, such a peak shift was not observed (Fig. 2a inset). It is possible that the bulk of $NiSi_2$ did not store Li and only the surface was alloyed with Li, but we did not have a method to distinguish the reaction point (bulk or surface) of the metal silicide. Thus, the fourth hypothesis (Fig. 1d) remains a possibility. Although the y value in Li_yNiSi_2 was estimated to be 2.1 for the capacity of 500 mA h g^{-1}, the y value becomes extremely large when only the surface is alloyed with Li.

3.5 Lithiation site of $NiSi_2$

We investigated the lithiation site of $NiSi_2$ using first-principles calculations. Figure 6 shows the optimized crystal structure of Li_yNiSi_2 for $y = 0.5$ (SOC: 20 %), 1.0 (SOC: 40 %), and 2.25 (SOC: 90 %). All the Li sites at SOCs of 20 % and 40 % were equivalent to the position of (x, y, z) = (0.5, 0.5, 0.5) and denoted by purple balls in Fig. 6, whereas those at an SOC of 90 % were classified into two inequivalent sites denoted by purple and blue balls in Fig. 6. The sites of the blue balls were equivalent to the position of (x, y, z) = (0.28, 0.5, 0.5). Although we also attempted to optimize the structures of $y = 1.5$ (SOC: 60 %) and 2.0 (SOC: 80 %), the calculation did not converge. The valence electron numbers of the Li sites were calculated using Bader analysis (Table 1). The NMR spectra at SOCs of 20 % and 40 % exhibited only one peak (Peak A in Fig. 5), whereas those at SOCs of 60 %–100 % showed two peaks (Peak A and B in Fig. 5). These results indicate that all of the Li sites at SOCs of 20 % and 40 % were equivalent, whereas those at SOCs of 60 %–100 % were divided into two equivalent sites, which corresponded to the optimized structures in Fig. 6.

The valence electron number of Li atom at SOCs of 20 % and 40 % was 0.20 (Table 1). In contrast, the valence electron number of Li atom at 90 % SOC was 0.16 and 0.29. The number 0.16, which is close to the original value of 0.20, was expected to belong to Peak A, and the number 0.29 was expected to belong to Peak B. Figure 5b shows that the peak area ratio at 100 % SOC was almost identical to the ratio of Li atoms. However, when the valence electron number was larger, the peak appeared at a higher magnetic field (lower chemical shift) in the NMR spectra, contradicting the result in Fig. 5a (Peak B with a larger valence electron number must appear on the right side of Peak A).

It has been reported that Li_xSi phases with low lithiation ($x =$ 1.71, 2.33, 3.25, and 3.75) are semiconductors, whereas $Li_{4.20}Si$ only occurs as a metallic phase. With an increase in conduction electrons near the Fermi level, the NMR peak of $Li_{4.20}Si$ appears at a lower magnetic field (higher chemical shift) than other Li_xSi phases, which is influenced by large Knight shifts.[36] Although $NiSi_2$ is metallic, Peak B could appear at a lower magnetic field than Peak A because of an increase in the conduction electrons. To estimate the change in the number of conduction electrons as y increases in Li_yNiSi_2, we investigated the charge transfer resistance using electrochemical impedance spectroscopy. However, there was no change in resistance as the SOC increased. Therefore, we calculated the total density of states (total DOS) and attempted to determine the number of conduction electrons near the Fermi level.

3.6 DOS analysis of Li_yNiSi_2

Figure S5 shows the total DOS of Li_yNiSi_2 ($y = 0$, 0.5, 1.0, 2.25, and 2.5) at 298 K. When the absolute temperature (T) of the system is sufficiently $\geq$0 K, the thermal energy excites electrons at levels below the Fermi energy (E_F), resulting in electrons above the E_F. In such cases, the energy distribution function of electrons ($f(E)$) is determined according to the Fermi–Dirac distribution function given by

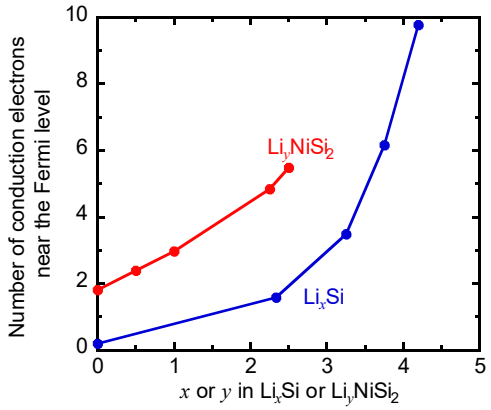

Figure 7. Change in number of conduction electrons near the Fermi level with an increase in x or y in Li_xSi or Li_yNiSi_2, respectively.

$$f(E) = \frac{1}{\exp\left(\frac{E - E_F}{k_B T}\right) + 1} \quad (6)$$

where k_B is the Boltzmann constant.[38] The electronic states in the energy range of $E_F - 0.25\,eV < E < E_F + 0.25\,eV$ were used to estimate the number of conduction electrons (Fig. S5). The results were 1.81, 2.40, 2.96, 4.84, and 5.49 for $y = 0$, 0.5, 1.0, 2.25, and 2.5 in Li_yNiSi_2, respectively (Fig. 7), confirming that the number of conduction electrons was an increasing function of y.

Knight shifts in the ^{7}Li NMR of $Li_{4.20}Si$ have only been reported among different Li_xSi phases. We confirmed the total DOS of different Li_xSi phases and compared them with that of Li_yNiSi_2. Figure S6 provides the DOS of Li_xSi ($x = 0$, 2.33, 3.25, 3.75, and 4.20) at 298 K, which was consistent with the trend found in the previous report.[39] The numbers of conduction electrons were estimated to be 0.20, 1.59, 3.47, 6.17, and 9.76 for $x = 0$, 2.33, 3.25, 3.75, and 4.20, respectively (Fig. 7). As in Li_yNiSi_2, the number of conduction electrons increased with an increase in the x value. Although Knight shifts have not previously been confirmed in $Li_{3.75}Si$ phase,[36,37] the number of conduction electrons was relatively high and the $Li_{3.75}Si$ seemed to be a metallic phase (Fig. S6d). However, the various Li_xSi ($x = 0$–3.75) phases have been reported to be semiconductors.[36,40–42] In contrast, because $NiSi_2$ was originally a metallic phase, it was assumed that a Knight shift occurred at an SOC of >60 %.

Although Peak B must appear at a higher magnetic field (lower chemical shift) than Peak A based on the valence electron numbers, it appeared at a lower magnetic field (higher chemical shift). This was caused by an increase in the number of conduction electrons near the Fermi level and the occurrence of Knight shifts. Therefore, Peaks A and B were assigned valence electron numbers of 0.16 and 0.29, respectively. Additionally, the Li storage sites of Peaks A and B corresponded to the purple and blue atomic positions in Fig. 6. As previously reported, the $FeSi_2$ electrode at 20 % SOC produced a shoulder derived from Peak B at approximately 11 ppm during the fifth cycle, and the intensity of Peak B increased with an increase in SOC.[28] For the $NiSi_2$ electrode, the lithiation site arising from Peak B is expected to be slightly different because the positions of Peak B and the SOCs at which Peak B appeared differed between $NiSi_2$ and $FeSi_2$.

4. Conclusions

We clarified the electrochemical lithiation mechanism of an $NiSi_2$ electrode. Four possible mechanisms were suggested, and each possibility was investigated in detail using XRD, Raman spectroscopy, TEM, EDS, and NMR. The results showed that there was no $NiSi_2$ phase separation and a pure Si phase was not generated; thus, lithiation of Si generated from $NiSi_2$ did not occur. Additionally, stable Li metal deposition–dissolution did not occur on the $NiSi_2$ electrode. Although the reaction point (bulk or surface) of the metal silicide remains unclear, electrochemical lithiation of the $NiSi_2$ itself proceeded. Furthermore, we determined the lithiation site in $NiSi_2$ using NMR analysis and first-principles calculations. At a lower SOC, there was only one lithiation site equivalent to $(x, y, z) = (0.5, 0.5, 0.5)$. At a higher SOC, Li atoms were stored at another site in the $NiSi_2$ crystal lattice, which was equivalent to $(x, y, z) = (0.28, 0.5, 0.5)$. The position of Peak B in the NMR spectra could not be explained by the valence electron numbers. However, the number of conduction electrons was examined based on the total DOS results and it was found that Knight shifts occurred. Therefore, the lithiation sites of Peaks A and B were elucidated.

Acknowledgments

TEM and EDS were performed at the NIMS Battery Research Platform. The authors thank Mr. K. Imanishi at Tottori University for his assistance with the XRD analysis. This study was partially supported by the Japan Society for the Promotion of Science (JSPS) KAKENHI (Grant numbers JP24K08565, JP20H00399, JP23K26758, JP23K04535, and JP23K18465) and NIMS Joint Research Hub Program.

CRediT Authorship Contribution Statement

Yasuhiro Domi: Conceptualization (Lead), Formal analysis (Equal), Funding acquisition (Equal), Writing – original draft (Lead), Writing – review & editing (Lead)
Hiroyuki Usui: Conceptualization (Lead), Funding acquisition (Supporting), Methodology (Supporting), Writing – original draft (Equal), Writing – review & editing (Equal)
Takumi Ando: Data curation (Lead), Formal analysis (Equal), Investigation (Lead), Writing – original draft (Equal), Writing – review & editing (Supporting)
Ryuto Tanaka: Data curation (Equal), Investigation (Equal), Methodology (Supporting), Writing – original draft (Supporting), Writing – review & editing (Equal)
Kazuma Gotoh: Conceptualization (Supporting), Data curation (Lead), Investigation (Equal), Methodology (Equal), Writing – review & editing (Supporting)
Takeo Hoshi: Conceptualization (Supporting), Data curation (Supporting), Investigation (Supporting), Methodology (Equal), Writing – review & editing (Equal)
Kei Nishikawa: Data curation (Supporting), Investigation (Supporting), Methodology (Supporting), Writing – review & editing (Supporting)
Hiroki Sakaguchi: Conceptualization (Equal), Funding acquisition (Lead), Methodology (Equal), Writing – original draft (Equal), Writing – review & editing (Supporting)

Data Availability Statement

The data that support the findings of this study are openly available under the terms of the designated Creative Commons License in J-STAGE Data listed in D1 of References.

Conflict of Interest

The authors declare no conflict of interest in the manuscript.

Funding

Japan Society for the Promotion of Science: JP24K08565
Japan Society for the Promotion of Science: JP20H00399
Japan Society for the Promotion of Science: JP23K04535
Japan Society for the Promotion of Science: JP23K18465
Japan Society for the Promotion of Science: JP23K26758

References

D1. Y. Domi, H. Usui, T. Ando, R. Tanaka, K. Gotoh, T. Hoshi, K. Nishikawa, and

H. Sakaguchi, *J-STAGE Data*, https://doi.org/10.50892/data.electrochemistry.28490150, (2025).
1. S. C. Lai, *J. Electrochem. Soc.*, **123**, 1196 (1976).
2. C. J. Wen and R. A. Huggins, *J. Solid State Chem.*, **37**, 271 (1981).
3. M. N. Obrovac and L. Christensen, *Electrochem. Solid-State Lett.*, **7**, A93 (2004).
4. M. N. Obrovac and L. J. Krause, *J. Electrochem. Soc.*, **154**, A103 (2007).
5. B. Liang, Y. Liu, and Y. Xu, *J. Power Sources*, **267**, 469 (2014).
6. X. Zuo, J. Zhu, P. Müller-Buschbaum, and Y.-J. Cheng, *Nano Energy*, **31**, 113 (2017).
7. P. Li, H. Kim, S. T. Myung, and Y.-K. Sun, *Energy Storage Mater.*, **35**, 550 (2021).
8. H. Zhao, H. Zuo, J. Wang, and S. Jiao, *J. Energy Storage*, **98**, 113125 (2024).
9. Y. Domi, H. Usui, M. Shimizu, Y. Kakimoto, and H. Sakaguchi, *ACS Appl. Mater. Interfaces*, **8**, 7125 (2016).
10. S. Yodoya, Y. Domi, H. Usui, and H. Sakaguchi, *ChemistrySelect*, **4**, 1375 (2019).
11. H. Sakaguchi, T. Iida, M. Itoh, N. Shibamura, and T. Hirono, *IOP Conf. Ser.: Mater. Sci. Eng.*, **1**, 012030 (2009).
12. H. Usui, K. Maebara, K. Nakai, and H. Sakaguchi, *Int. J. Electrochem. Sci.*, **6**, 2246 (2011).
13. Y. Domi, H. Usui, H. Itoh, and H. Sakaguchi, *J. Alloys Compd.*, **695**, 2035 (2017).
14. Y. Domi, H. Usui, A. Ueno, Y. Shindo, H. Mizuguchi, T. Komura, T. Nokami, T. Itoh, and H. Sakaguchi, *J. Electrochem. Soc.*, **167**, 040512 (2020).
15. Y. Domi, H. Usui, E. Nakabayashi, Y. Kimura, and H. Sakaguchi, *ACS Appl. Energy Mater.*, **3**, 7438 (2020).
16. Y. Domi, H. Usui, T. Okasaka, K. Nishikawa, and H. Sakaguchi, *J. Electrochem. Soc.*, **171**, 080506 (2024).
17. Y. Domi, H. Usui, D. Iwanari, and H. Sakaguchi, *J. Electrochem. Soc.*, **164**, A1651 (2017).
18. Y. Domi, H. Usui, N. Ieuji, K. Nishikawa, and H. Sakaguchi, *ACS Appl. Mater. Interfaces*, **13**, 3816 (2021).
19. Y. Domi, H. Usui, K. Yamaguchi, S. Yodoya, and H. Sakaguchi, *ACS Appl. Mater. Interfaces*, **11**, 2950 (2019).
20. Y. Domi, H. Usui, A. Ando, K. Nishikawa, and H. Sakaguchi, *ACS Appl. Energy Mater.*, **3**, 8619 (2020).
21. Y. Domi, H. Usui, K. Nishikawa, and H. Sakaguchi, *ACS Appl. Nano Mater.*, **4**, 8473 (2021).
22. Y. Domi, H. Usui, R. Takaishi, and H. Sakaguchi, *ChemElectroChem*, **6**, 581 (2019).
23. Y. Domi, H. Usui, T. Ando, and H. Sakaguchi, *Mater. Adv.*, **3**, 6231 (2022).
24. G. X. Wang, L. Sun, D. H. Bradhurst, S. Zhong, S. X. Dou, and H. K. Liu, *J. Power Sources*, **88**, 278 (2000).
25. Y.-N. Zhou, W.-J. Li, H.-J. Chen, C. Liu, L. Zhang, and Z. Fu, *Electrochem. Commun.*, **13**, 546 (2011).
26. Z. Du, T. D. Hatchard, P. Bissonnette, R. A. Dunlap, and M. N. Obrovac, *J. Electrochem. Soc.*, **163**, A2456 (2016).
27. A. K. Niessen, P. R. de Boer, R. Boom, P. F. de Châtel, W. C. M. Mattens, and A. R. Miedema, *Calphad*, **7**, 51 (1983).
28. Y. Domi, H. Usui, K. Sugimoto, K. Gotoh, K. Nishikawa, and H. Sakaguchi, *ACS Omega*, **5**, 22631 (2020).
29. H. A. Ambjörnsson, K. Schenzel, and U. Germgård, *BioResources*, **8**, 1918 (2013).
30. M. Shimizu, H. Usui, T. Suzumura, and H. Sakaguchi, *J. Phys. Chem. C*, **119**, 2975 (2015).
31. O. Pecher, J. Carretero-González, K. J. Griffith, and C. P. Grey, *Chem. Mater.*, **29**, 213 (2017).
32. K. Gotoh, T. Yamakami, I. Nishimura, H. Kometani, H. Ando, K. Hashi, T. Shimizu, and H. Ishida, *J. Mater. Chem. A*, **8**, 14472 (2020).
33. B. M. Meyer, N. Leifer, S. Sakamoto, S. G. Greenbaum, and C. P. Grey, *Electrochem. Solid-State Lett.*, **8**, A145 (2005).
34. A. Budi, A. Basile, G. Opletal, A. F. Hollenkamp, A. S. Best, R. J. Rees, A. I. Bhatt, A. P. O'Mullane, and S. P. Russo, *J. Phys. Chem. C*, **116**, 19789 (2012).
35. D. M. Piper, T. Evans, K. Leung, T. Watkins, J. Olson, S. C. Kim, S. S. Han, V. Bhat, K. H. Oh, D. A. Buttry, and S.-H. Lee, *Nat. Commun.*, **6**, 6230 (2015).
36. B. Key, R. Bhattacharyya, M. Morcrette, V. Seznéc, J. M. Tarascon, and C. P. Grey, *J. Am. Chem. Soc.*, **131**, 9239 (2009).
37. B. Key, M. Morcrette, J. M. Tarascon, and C. P. Grey, *J. Am. Chem. Soc.*, **133**, 503 (2011).
38. P. H. Chavanis and J. Sommeria, *Mon. Not. R. Astron. Soc.*, **296**, 569 (1998).
39. V. L. Chevrier, J. W. Zwanziger, and J. R. Dahn, *J. Alloys Compd.*, **496**, 25 (2010).
40. R. Nesper, *Prog. Solid State Chem.*, **20**, 1 (1990).
41. H. G. von Schnering, R. Nesper, J. Curda, and K. F. Tebbe, *Angew. Chem.*, **92**, 1070 (1980).
42. R. Nesper and H. G. von Schnering, *J. Solid State Chem.*, **70**, 48 (1987).